Numerical modeling of three-dimensional stratified tidal flow over Camarinal Sill, Strait of Gibraltar

J. C. Sánchez-Garrido,[1] G. Sannino,[2] L. Liberti,[3] J. García Lafuente,[1] and L. Pratt[4]

Received 2 March 2011; revised 10 September 2011; accepted 7 October 2011; published 17 December 2011.

[1] The baroclinic response to barotropic tidal forcing in the Camarinal Sill area, within the Strait of Gibraltar, is investigated with a three-dimensional, fully nonlinear, nonhydrostatic numerical model. The aim of numerical efforts was the assessment of three-dimensional effects, which are potentially significant in the area because of rather irregular bottom topography, variable background stratification, and complex structure of barotropic tides. Model results reveal a complex baroclinic response under relatively moderate flood tidal currents, which includes the formation of internal hydraulic jumps upstream of the sill, internal cross waves close to the channel walls, and a plunging pycnocline at the lee side of the sill crest. These structures exhibit significant cross-channel spatial dependence and may appear to be aligned together across the channel. This fact makes their identification difficult from the surface pattern captured by remote sensing images. Under strong barotropic forcing (spring tides) the upstream hydraulic jumps are shifted to the lee side of Camarinal Sill, where a single internal hydraulic jump is formed. Significant first- and second-mode hydraulic jumps are also generated near smaller secondary sills in Tangier basin, thus extending the occurrence of intense water mixing and energy dissipation to other zones of the strait.

Citation: Sánchez-Garrido, J. C., G. Sannino, L. Liberti, J. García Lafuente, and L. Pratt (2011), Numerical modeling of three-dimensional stratified tidal flow over Camarinal Sill, Strait of Gibraltar, *J. Geophys. Res.*, *116*, C12026, doi:10.1029/2011JC007093.

1. Introduction

[2] The Strait of Gibraltar is a prominent spot of the World Ocean connecting the Mediterranean Sea and the Atlantic Ocean through a narrow channel (minimum width of 14 km) characterized by an irregular bottom topography that includes a system of submarine sills (see Figures 1 and 2). Buoyancy losses over the Mediterranean Sea lead to a two-way (or baroclinic) exchange in the strait [*Bryden and Kinder*, 1991], in which approximately 0.8 Sv (1 Sv = 10^6 m^3 s^{-1}) of salty and dense Mediterranean Water (MW) flows toward the Atlantic in the bottom layer, and a slightly higher volume rate of Atlantic Water (AW), about 0.85 Sv, enters the Mediterranean in the surface layer to compensate for the net evaporative losses over the basin.

[3] The exchange flow is far from being steady. It fluctuates at very different timescales exhibiting tidal, meteorological, seasonal, and interannual [see, e.g., *Candela et al.*, 1989; *García Lafuente et al.*, 2007]. Among all these scales the tidal band is by far the most energetic, with tidal flow exceeding 5 Sv [*García Lafuente et al.*, 2000] and masking the underlying mean baroclinic exchange during important part of the tidal cycle. Furthermore, interaction of flood tidal currents (tidal flow toward the Atlantic) with Camarinal Sill (CS; see Figures 1 and 2), the main sill of Gibraltar, leads to the periodic generation of large-amplitude internal waves (LAIWs) with amplitude exceeding 100 m [*Ziegenbein*, 1969; *Richez*, 1994]. After their generation LAIWs propagate eastward carrying a large amount of baroclinic energy that is eventually transferred to turbulence and mixing especially in shallow areas where wave breaking occurs. Consequently these waves play a relevant role in the oceanography of the Strait of Gibraltar and Alboran Sea ecosystems.

[4] Observational evidence [*Farmer and Armi*, 1988; *Armi and Farmer*, 1988] and numerical results [*Brandt et al.*, 1996; *Vázquez et al.*, 2006] show that LAIWs are the result of the nonlinear evolution of a baroclinic bore (or moving hydraulic jump) generated at CS. Under critical flow conditions the baroclinic bore is trapped in CS until nearly high tide when the barotropic tidal flow weakens. At this time the bore progresses eastward through the strait to the Alboran Sea while transforming into a series of internal solitary waves by nonlinear and dispersive (nonhydrostatic) effects. This process of wave evolution in a dispersive media is well

[1] Grupo de Oceanografía Física, Departamento Física Aplicada II, University of Malaga, Malaga, Spain.
[2] Ocean Modeling Unit, Ente per le Nuove Tecnologie, l'Energia e l'Ambiente, Rome, Italy.
[3] Istituto Superiore per la Protezione e la Ricerca Ambientale, Rome, Italy.
[4] Woods Hole Oceanographic Institution, Woods Hole, Massachusetts, USA.

0148-0227/11/2011JC007093

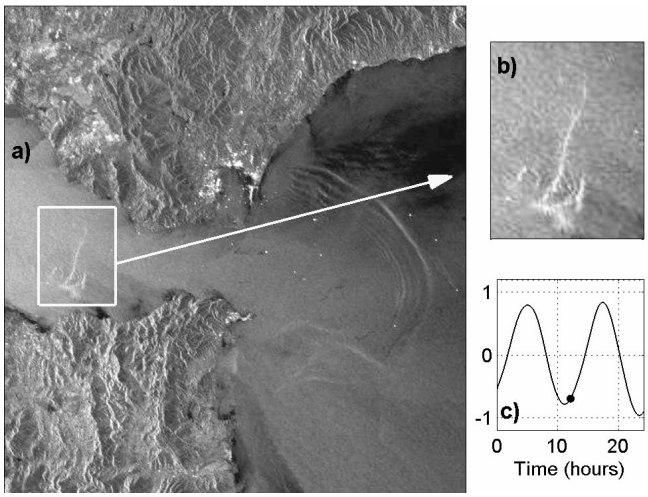

Figure 1. (a) Synthetic aperture radar (SAR) image of the Strait of Gibraltar showing the developing internal waves in Camarinal Sill (CS) and the propagation of a previously generated packet of large-amplitude internal waves (LAIWs) in the Alboran Sea (date of reception: 28 November 2005, 22:09; Envisat ASAR data were provided by the European Space Agency). (b) Detail of CS area. (c) Barotropic current velocity (depth-averaged velocity) prediction over CS (5°44.64′W, 36°54.78′N) at the time of the image.

known and has been documented in many works dealing with weakly nonlinear wave theories [*Whitham*, 1974].

[5] Although the overall generation mechanism of LAIWs in Gibraltar is well understood, there are some important aspects not yet addressed in numerical studies.

[6] 1. Numerical models considered laterally averaged (cross-strait) governing equations, thus missing transversal effects associated with across-channel variations of barotropic forcing, background stratification, and bottom topography. These effects are assumed to play a minor role in narrow channels of the World Ocean such as the Strait of Messina in the central Mediterranean [*Brandt et al.*, 1997], or a number of stratified fjords [*Armi and Farmer*, 2002] where tidally generated LAIWs also occur. Transversal effects are however likely to be significant in the Strait of Gibraltar, where the internal Rossby radius of deformation is comparable to the strait width, originating a nonnegligible cross-strait variation of isopycnal depth (increasing southward), and both surface (barotropic) tides and bottom topography have a complex structure with important across-channel variations [*García Lafuente et al.*, 1990; *Candela et al.*, 1990]. In fact, available synthetic aperture radar (SAR) images of CS area like the one presented in Figure 1 sometimes suggest the three-dimensionality of the baroclinic wavefield. The image was taken at the time when barotropic (depth-averaged) tidal velocity nearly reached its maximum toward the Atlantic (Figure 1c), when presumably the baroclinic bore has not yet been released. Instead of the expected single wavefront, two fronts can be observed in CS area. The front located downstream (to the west) appears in the image almost as a straight line extending all across the strait, but the one located upstream is confined to the southern half of the section.

[7] 2. The previously mentioned models were forced only by the M_2 tidal constituent. Although this is the most important one, other constituents account for a significant portion of the barotropic energy (S_2, O_1, K_1), and determine clear modulation of the strength of the LAIW packets as observed by *Sánchez-Garrido et al.* [2008]. In fact, M_2 barotropic transport is estimated in 3 Sv [*García Lafuente et al.*, 2000], whereas during spring tides tidal transport can be almost twice that amount. Important differences in the baroclinic response are then expected throughout the neap-spring cycle.

[8] This paper presents a numerical investigation on the generation of LAIWs in the Strait of Gibraltar with emphasis on three-dimensional aspects of the generated wavefield. We use a high-resolution, three-dimensional, fully nonlinear and nonhydrostatic model which reproduces the mean two-way exchange of the strait and it is forced by a realistic barotropic tide simulating the neap-spring cycle. Model features and initialization are described in section 2, model results for tidal cycles of increasing strength are discussed in section 3, and a summary and conclusions are presented in section 4.

2. Model Description and Initialization

[9] The Massachusetts Institute of Technology general circulation model (MITgcm) has been used for this work. The MITgcm solves the fully nonlinear, nonhydrostatic Navier–Stokes equations under the Boussinesq approximation for an incompressible fluid with a spatial finite-volume discretization on a curvilinear computational grid. The model formulation, which includes implicit free surface and partial step topography, is described in detail by *Marshall et al.* [1997a, 1997b] and its source code and documentation are available at the MITgcm Group Web site (http://mitgcm.org/sealion/online_documents/node2.html).

[10] The model domain extends from 6.3°W to 4.78°W and was discretized by a nonuniform curvilinear orthogonal grid of 1440 × 210 points (Figure 2a). Spatial resolution along the longitudinal axis of the strait, Δx, (across the strait axis, Δy,) ranges between 46 and 63 m (175–220 m) in the CS area and mesh size is always less than 70 m (340 m) in the middle of the strait between Espartel Sill (the westernmost sill of Gibraltar, hereinafter ES) and CS, and less than 70 m (200 m) between CS and Tarifa Narrows, the narrowest section of the strait. To adequately resolve the pycnocline the model has 53 vertical z levels with a thickness of 7.5 m in the upper 300 m gradually increasing to a maximum of 105 m for the remaining 13 bottom levels.

[11] Model topography (Figures 2b and 2c) has been obtained by merging the ETOPO2 bathymetry [*NOAA*, 2006] with the very high resolution bathymetry chart of [*Sanz et al.*, 1991]. No-slip conditions were imposed at the bottom and lateral solid boundaries.

[12] The selected tracer advection scheme is a third-order direct space-time flux limited scheme [*Hundsdorfer et al.*, 1995], which is unconditionally stable and does not require additional diffusion. Following the numerical experiments conducted by *Vlasenko et al.* [2009] to investigate the 3-D

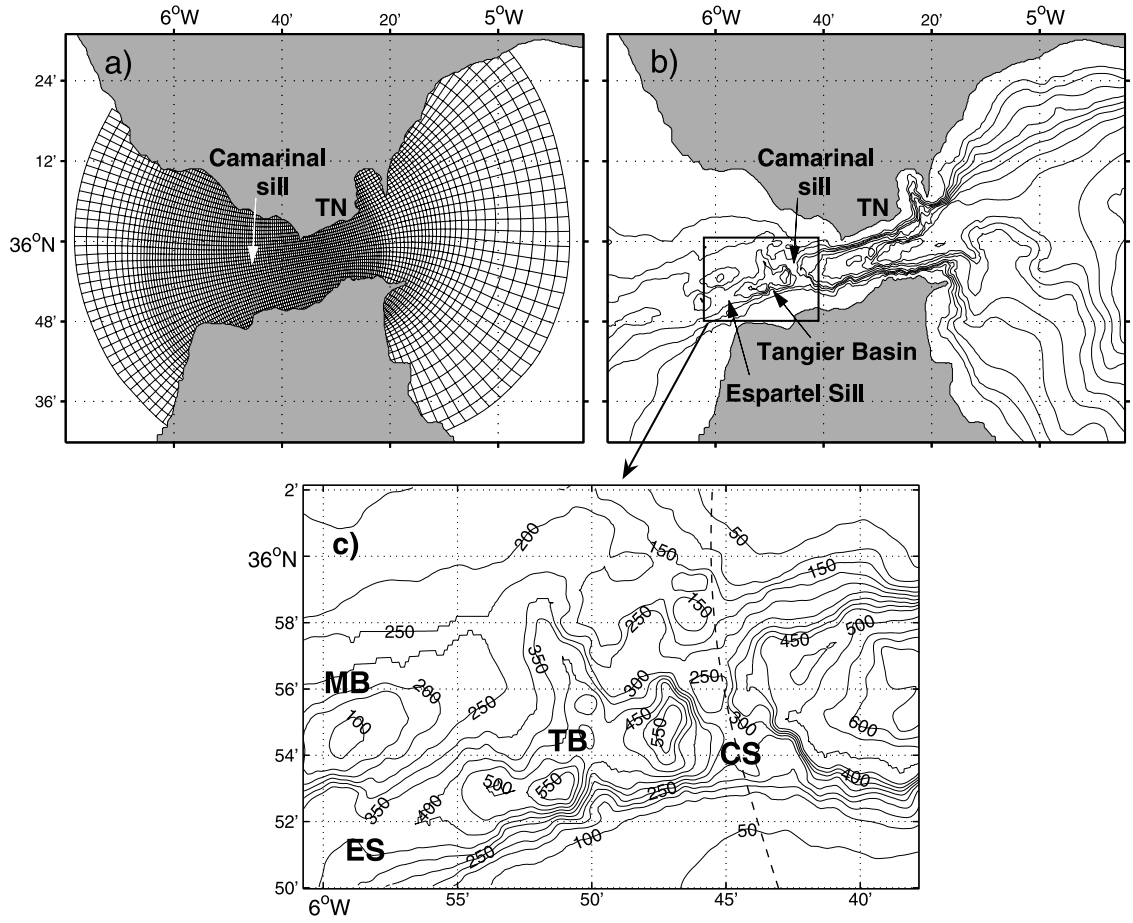

Figure 2. (a) Computational grid used in the numerical experiment (for the sake of clarity, only 2% of the grid points are shown). The locations of Camarinal Sill and Tarifa Narrows (TN) are indicated. (b) Bottom topography of the Strait of Gibraltar (isobaths are shown every 100 m). (c) Detailed bottom topography map in the area of the Camarinal Sill (CS), Tangier Basin (TB), Espartel Sill (ES), and Majuan Bank (MB). Dashed line indicates the cross-strait section over CS.

evolution of LAIWs in the Strait of Gibraltar, the turbulent closure parametrization for vertical viscosity and diffusivity proposed by *Pacanowski and Philander* [1981]

$$\nu = \frac{\nu_0}{(1+\alpha Ri)^n} + \nu_b, \quad \kappa = \frac{\nu}{(1+\alpha Ri)} + \kappa_b, \tag{1}$$

was used, where $Ri = N^2(z)/(u_z^2 + v_z^2)$ is the Richardson number, $\nu_b = 1.5 \times 10^{-4}$ m^2 s^{-1}, $\kappa_b = 1 \times 10^{-7}$ m^2 s^{-1} are background values, and $\nu_0 = 1.5 \times 10^{-2}$ m^2 s^{-1}, $\alpha = 5$ and $n = 1$ are adjustable parameters. Horizontal diffusivity coefficient is $\kappa_h = 1 \times 10^{-2}$ m^2 s^{-1}, whereas variable horizontal viscosity follows the parameterization of *Leith* [1968].

[13] Initial conditions for temperature and salinity were derived from the climatologic Medar-MedAtlas Database [*MEDAR Group*, 2002] for the month of April. The mean two-way exchange is obtained by laterally forcing the model through the imposition of the mean baroclinic velocities and tracers extracted from the intermediate resolution model developed by *Sannino et al.* [2009] to study the water exchange through the strait and its hydraulic behavior. Therefore, the present model can be viewed as a nested model of the one described by *Sannino et al.* [2009]. The model initially ran for 11 days without tidal forcing in order to reach a quasi-steady two-way exchange. Subsequently, tidal forcing was introduced by prescribing at the open boundaries the main diurnal (O_1, K_1) and semidiurnal (M_2, S_2) barotropic tidal currents, extracted from the intermediate resolution model. The simulation was then extended for 8 more days in order to attain a stable time periodic solution. Finally, the actual numerical experiment was carried out by running the model for a full tropical month. Wave reflections at the open boundaries are minimized by adding a Newtonian relaxation term to the tracer equations over the boundary area and adopting the flow relaxation scheme proposed by *Carter and Merrifield* [2007] for the velocity field.

[14] The most apparent difference between the intermediate and the nested model results concerns diapycnal mixing, which is better simulated in the latter because of its higher spatial resolution and nonhydrostatic formulation (the impact of a more realistic representation of water mixing on the exchange flow and hydraulics of the strait will be the subject of a future work). Mean and barotropic tidal currents obtained in the present numerical experiment are similar to the ones obtained in the intermediate model, which in turn

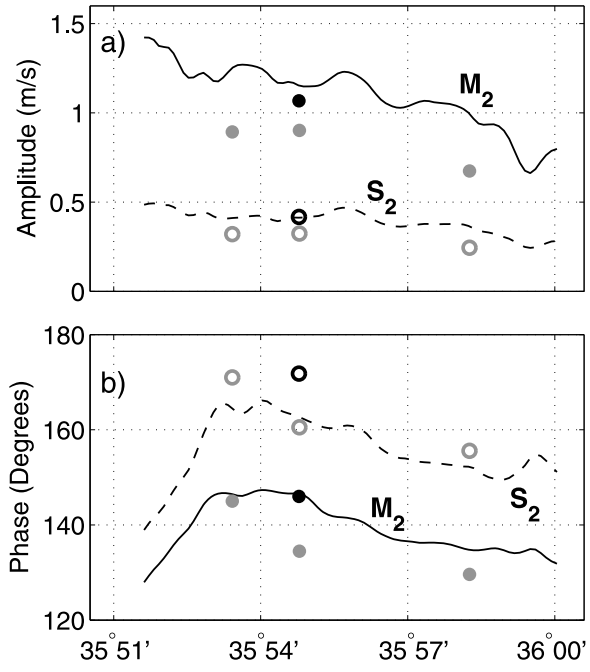

Figure 3. (a) Semidiurnal (solid line, M_2; dashed line, S_2) tidal amplitudes of barotropic currents in the CS cross section (dashed line in Figure 2c). Gray symbols correspond to observations reported by *Candela et al.* [1990], and black symbols correspond to acoustic Doppler current profiler (ADCP) observations collected within the INGRES projects (see text for details). Dots (circles) indicate the amplitude of tidal constituent M_2 (S_2). (b) Same as Figure 3a for tidal phases.

were in good agreement with historical observations collected in the strait [*Sánchez-Román et al.*, 2009]. Example of the good performance of the model is provided in Figure 3, which shows semidiurnal tidal amplitudes and phases of modeled barotropic tidal currents across CS along with depth-averaged values of harmonic tidal analysis presented by *Candela et al.* [1990]. Amplitudes and phases increase toward the south both in numerical outputs and observations, although M_2 amplitudes are somewhat higher in the model results. Much better agreement is found with acoustic Doppler current profiler (ADCP) observations encompassing nearly the whole water column over CS (black dots; see data set description by *García Lafuente et al.* [2007]), suggesting that the lack of information in the upper layer in the data presented by *Candela et al.* [1990] is the source of discrepancy.

3. Models Results

[15] Model results reveal that nonlinear internal waves propagating as internal bores and solitary waves develop for a maximum barotropic tidal transport $Tr_{max} > 3.0$ Sv, approximately the tidal transport associated with the M_2 tidal constituent. Our analysis focuses on this upper range of tidal forcing, which has been split into two different cases considering qualitatively different baroclinic response over CS.

3.1. Moderate Tidal Forcing

3.1.1. Two-Dimensional Surface Pattern Produced by the Baroclinic Field

[16] We start our analysis by examining the less energetic case looking at a tidal cycle characterized by $Tr_{max} = 3.65$ Sv, which can be classified as a moderate tidal forcing cycle. An effective procedure to trace the evolution of the internal or baroclinic field consists of monitoring the spatial gradient of surface velocity. The superposition of baroclinic and barotropic currents gives rise to areas of strong horizontal convergence/divergence of the flow characterized by short-scale surface roughness which can be captured by SARs [*Alpers*, 1985]. This allows for the identification of baroclinic structures such as internal hydraulic jumps or free propagating internal waves through the observation of the ocean surface.

[17] Figure 4 shows the surface zonal velocity gradient evolution in the sills area of the strait during the flood tide. Figure 4a corresponds to the beginning of the flood tide, when barotropic tidal flow over CS is null. In spite of this, two noticeable surface signatures appear in shallow areas nearby CS close to the channel walls. The one in the north is especially significant, resembling a wavefront that extends over great distance roughly along $z = 50$ m isobath. Minor surface signatures can be also observed in the proximity of Majuan Bank (~6°57′W, 36°55′N, Figure 2), the seamount immediately north ES. The origin of these local features is analyzed in detail later.

[18] The surface pattern looks more complex when the barotropic flow increases (Figure 4b). In addition to some residual features in shallow areas to the north, two structures emerge in the centre of the channel, which at the moment of maximum tidal flow evolve into a pair of wavefronts (Figure 4c). One of them appears next to the $\theta = 5°45'$W meridian and encompasses almost the entire channel width, whereas the second, located further upstream, leaves a clearer trace at the south of the strait. The pattern clearly resembles the SAR image shown in Figure 1.

[19] The subsequent evolution corresponds to the relaxation of the tidal forcing. Weakening of the barotropic tidal flow triggers the release of the longer wavefront that propagates eastward under the effect of wave dispersion, as shown by the appearance of a dispersive wave tail (Figures 4d–4f). The front generated upstream however remains almost stationary and as a result eventually collides with the wave propagating behind (Figure 4e). Despite this complex evolution the wavefield finally entering Tarifa Narrows is a rather regular wave packet of LAIWs (Figure 4f).

[20] The last remark about Figure 4 concerns the small-scale structures generated west of CS, immediately downstream of the main wavefront (Figures 4b and 4c). They arise only at the time of maximum tidal flow, and vanish as soon as the flow slackens. Another interesting feature is the slanted front moving together with the main wave train close to the south channel wall (Figures 4d–4f).

3.1.2. Baroclinic Wavefield Over CS

[21] In this section we analyze in detail the baroclinic field generated over CS. Figure 5 provides a first insight into the internal wavefield by depicting the evolution of the isopycnal $\sigma_\theta = 27.5$ (approximately coincident with the

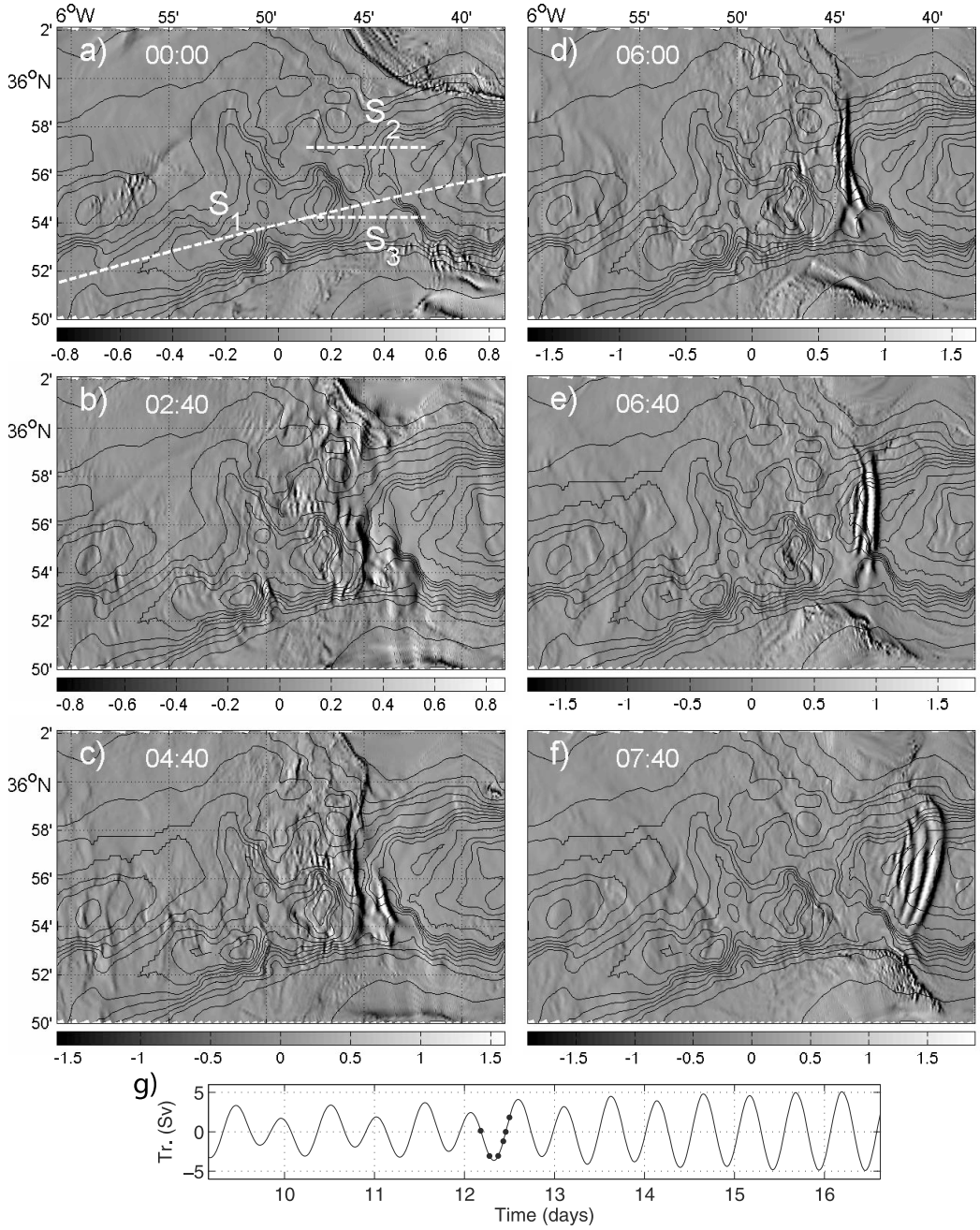

Figure 4. (a–f) Time evolution of surface zonal velocity gradient ($\times 10^{-3}$ s^{-1}) during the flood tide. Solid lines represent bottom depth contours (isobaths 50, 100, 150 m, etc.). The time origin is taken at the beginning of the flood tide. Dashed lines S_1, S_2, and S_3 in Figure 4a indicate cross sections mentioned in the text. (g) Barotropic tidal transport during the time series.

pycnocline) along zonal sections S_2 and S_3 (Figure 4a). Section S_3 covers the south central part of the channel, where two prominent surface features appear as flood current increases (Figure 4b), i.e., the southern portion of the longer front over the sill crest, and the shorter front generated further upstream. Figure 5a reveals that these two surface signatures are caused by a double plunge of isopycnals, the first over the western flank of the sill (feature A; ~5°45′W) and the second over the lee side of a 50 m bump situated at the eastern edge of the sill crest (feature B; ~5°43′W).

[22] Figure 5b shows a more complex baroclinic structure, with the formation of two upstream internal hydraulic jumps. One appears in the northern section S_2 (feature C; Figure 5b) aligned along θ = 5°45′W with the southern plunging pycnocline formed at the lee side of the sill. These two baroclininc structures are merged together in a single feature that forms the westernmost surface signature presented in

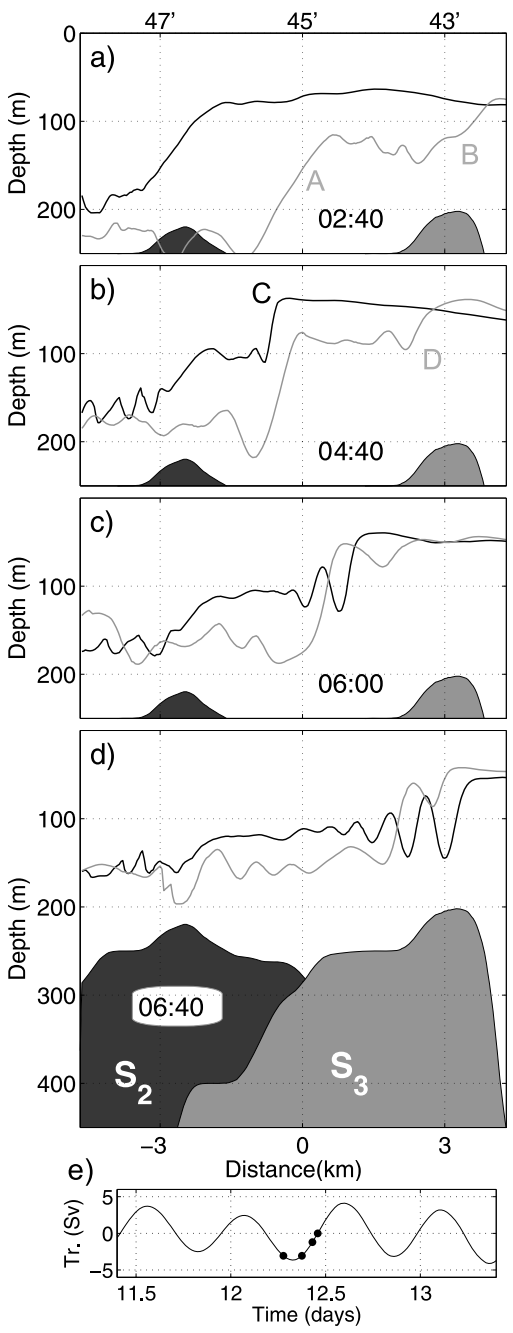

Figure 5. (a–d) Time evolution of σ_θ = 27.5 isopycnal along cross sections S_2 (black) and S_3 (gray) shown in Figure 4a. Features A, B, C, and D indicate baroclinic features mentioned in the text. The bottom axis indicates distance (km) from the center of Camarinal Sill, whereas the axis on the top indicates minutes to the west of the meridian 5°W. (e) Barotropic tidal transport during the time series.

Figure 4c and the SAR image of Figure 1. The second hydraulic jump is formed at the south section S_3 over the eastern edge of the sill (feature D; Figure 5b). Weakening of the tidal flux leads to the release of both the southern plunging pycnocline and the northern upstream hydraulic jump, which gradually disintegrates into a series of solitary-like internal waves. The hydraulic jump at the southeast edge of the sill crest also progresses eastward with slack currents, but much slower than the waves propagating behind, and is eventually absorbed by them (Figures 5c and 5d).

[23] Let us now analyze in more detail the fronts formed in the proximity of the channel walls. They can be distinguished throughout the whole flood period, even when the net tidal flux is null. Barotropic tidal velocities can be locally strong in coastal areas, even though the total tidal flow is weak. This can be seen in Figure 6b, which shows the barotropic velocity at the beginning of the flood tide. Velocities are small in the centre of the channel, but they are relatively large near the lateral boundaries of the channel, where the circulation is characterized by short-scale eddies. The stratification is generally weak in these shallow areas, although occasionally, a layer of relatively dense water can be present, as is shown in Figure 7 where a tongue of interface water (salinity ~37, mixture of Atlantic and Mediterranean waters) of 15–20 m thick intrudes onto the northern shelf beneath the Atlantic surface water (salinity ~36–36.5). If the stratified flow is simplified to a two-layer system, relatively large current velocities, weak stratification, and thin layers result in a locally supercritical flow in coastal areas (see shaded contours in Figures 6c and 6f). The assessment of the flow criticality is made in terms of the composite Froude number G^2 for a two-layer flow [*Armi*, 1986]:

$$G^2 = F_1^2 + F_2^2, \tag{2}$$

where $F_n = (u_n^2 + v_n^2)/(g'D_n)$; u_n, v_n and D_n are horizontal components of velocity and thickness of layer n, and g' the reduced gravity. The interface in the two-layer approximation of the stratified flow is taken as the depth of maximum vertical density gradient, whereas u_n, ρ_n are obtained by averaging velocity and density in layer n.

[24] Therefore, the lateral wavefronts can be thought of as oblique internal hydraulic jumps or stationary cross waves that can only exist where the flow is "locally supercritical". Here an analogy can be drawn with supercritical open-channel flows where cross waves are formed close to the lateral boundaries as a result of the turning effect produced by curved walls [*Chow*, 1959]. Although near the coast the flow remains supercritical almost permanently, cross waves only become apparent when the stratification is significant; that is to say, when the tongue of dense water intrudes onto shallow areas. They mainly appear in the northern part of the channel during the early stage of the tidal cycle because the pycnocline is shallow there (because of the Earth's rotation). It is during the ebb tide that cross waves are clear near the south coast (Figures 4d–4f), when the dense layer has been able to flood the southern shelf as a result of the overall rising of isopycnals produced by flood tidal currents (see Figure 8).

[25] The map of local G^2 deserves further discussion (Figure 6c). The flow is locally supercritical in marginal areas, but also downstream the western flank of the sill crest, where the Mediterranean undercurrent accelerates downslope (see also Figure 8a). This configuration is similar to a crest-controlled flow, where a subcritical-to-supercritical hydraulic transition occurs just over the sill crest; the flow then turns to supercritical along the western slope of the obstacle, and recovers the subcritical state in Tangier Basin (the basin separating Camarinal and Espartel sills, Figures 2b and 2c, hereinafter TB) through an internal

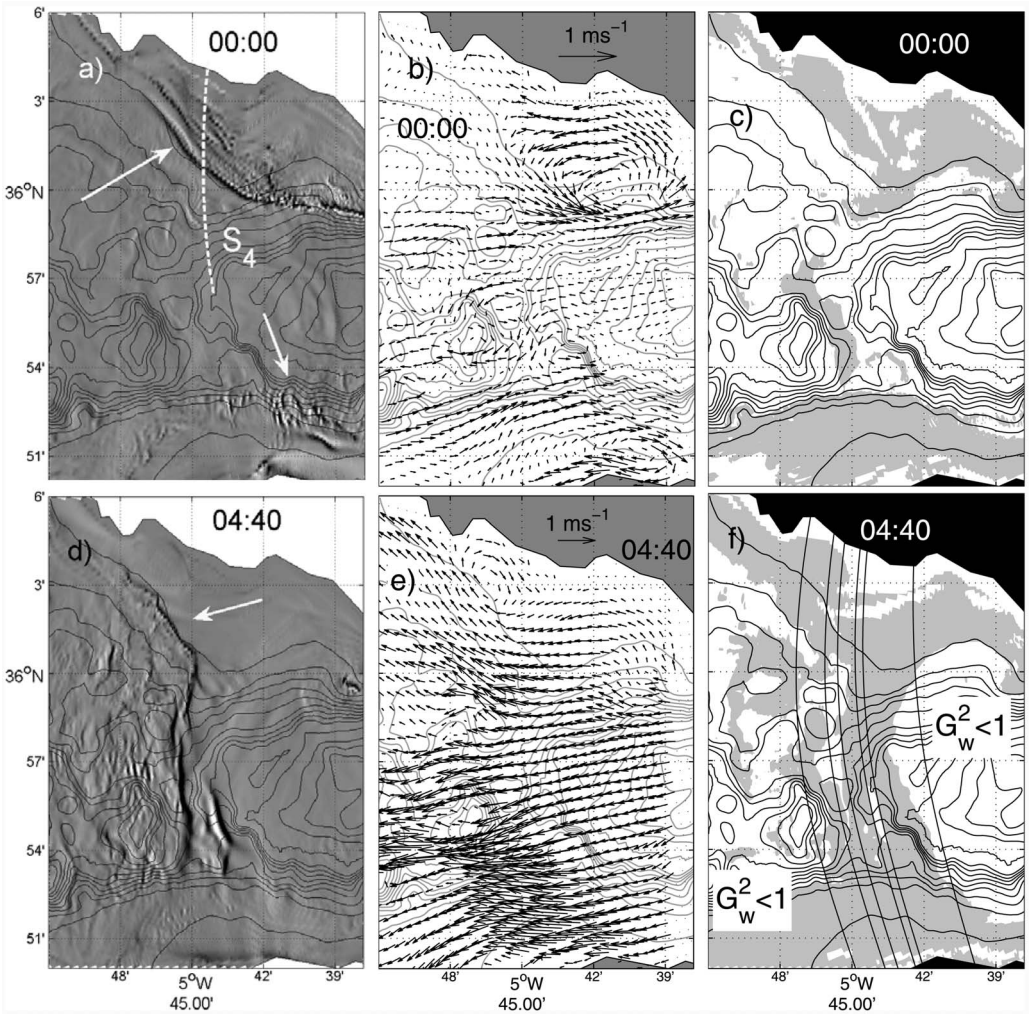

Figure 6. (a) Close up of the surface velocity gradient ($\times 10^{-3}$ s^{-1}) in CS area at t = 00:00 (see Figure 4a). Arrows indicate the position of cross waves. (b) Barotropic current velocity field at t = 00:00. (c) Criticality of the flow at t = 00:00. Shaded (unshaded) areas indicate local internal supercritical (subcritical) flow. (d–f) Same as Figures 6a–6c at t = 04:40. Transversal lines in Figure 6f indicate locations of hydraulic transitions according to the generalized composite internal Froude number for a two-layer flow (G_w^2 = 1).

hydraulic jump. Increase of tidal flow originates a control section well upstream of the sill at the eastern proximity of the obstacle (∼5°40′W, see shaded contour across the channel in Figure 6f). Moving downstream the flow then switches again to subcritical upstream of the sill, according to the subcritical patch encompassing the central northern part of the channel at ∼5°44′W. This supercritical-to-subcritical hydraulic transition corresponds to the abrupt drop in isopycnal height "C" shown in Figure 5b, supporting the idea that the feature in question is a hydraulic jump. Further downstream the flow becomes supercritical close to the sill crest, to finally turn to subcritical in TB.

[26] The above hydraulic analysis is local and does not speak to the question of overall control of the exchange flow. The value of G^2 at any point may give information about localized disturbances (as shown in the Appendix A), $G^2 \geq 1$ is a necessary condition for the existence of local cross waves, provided that the upper and lower layer velocity are more or less parallel. On the other hand the hydraulic of the flow as a whole depends on its properties over the entire cross section in question and involves wave with a cross-strait modal structure. The judgment of the flow criticality as a whole is based on the generalized composite Froude number G_w^2, considering transversal variations of

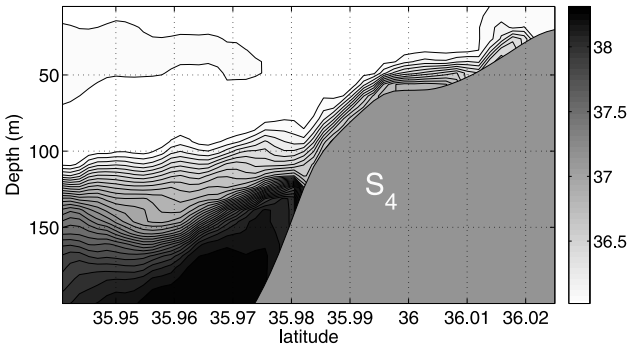

Figure 7. Salinity field along cross section S_4 (see Figure 6a) at t = 00:00.

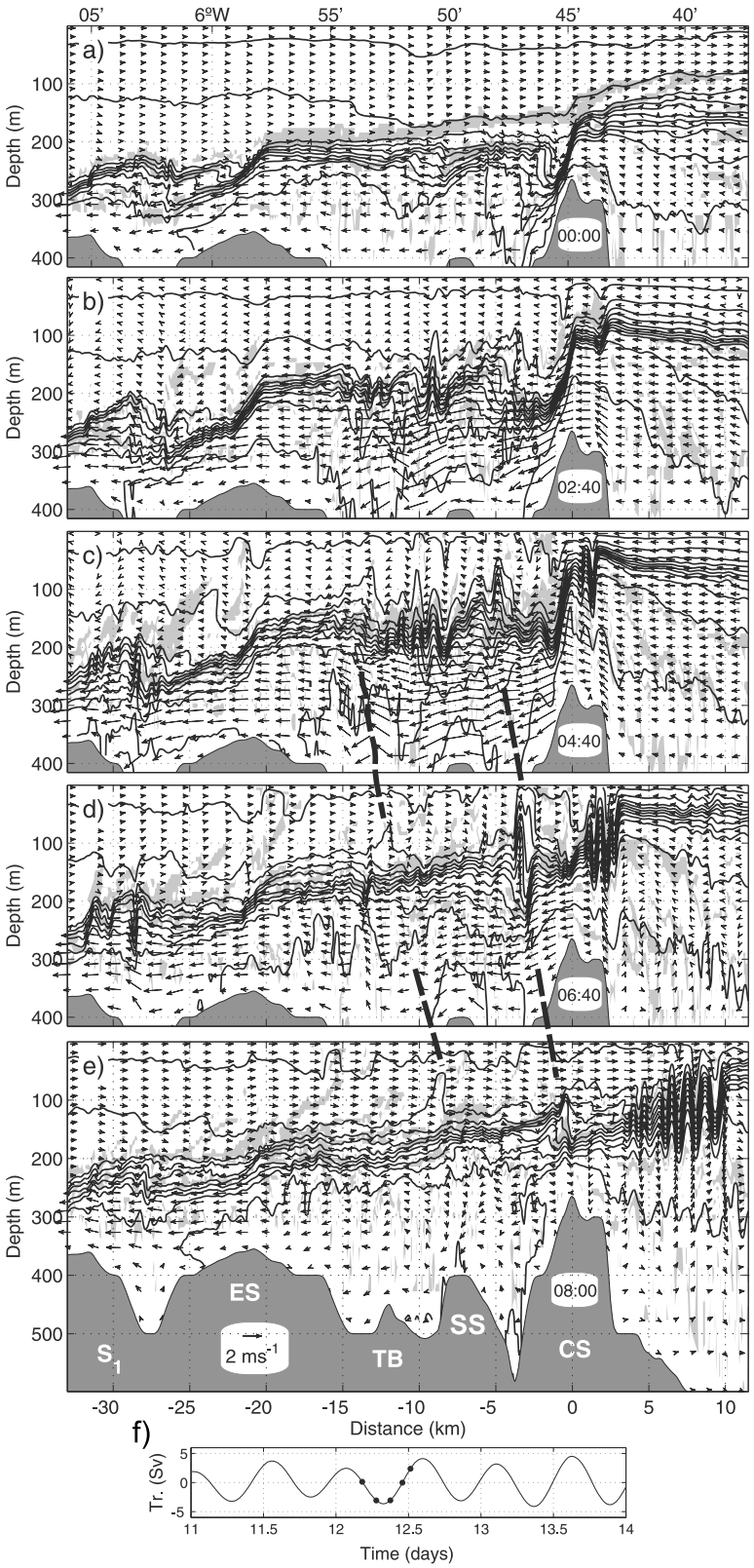

Figure 8. (a–e) Time evolution of the potential density field along the central axis of the strait (cross section S_1 in Figure 4) during moderate tidal cycle. Isopycnals σ_θ = 26.80,27.05,…,28.80,29.02 are shown. Arrows indicate local current velocity. Shaded contours are areas where $Ri < 1/4$, which are prone to the development of shear instabilities and occurrence of water mixing. Dashed thick lines indicate the evolution of two second-mode baroclinic bores. Feature SS in Figure 8e indicates the location of the secondary sill mentioned in the text. (f) Barotropic tidal transport during the time series.

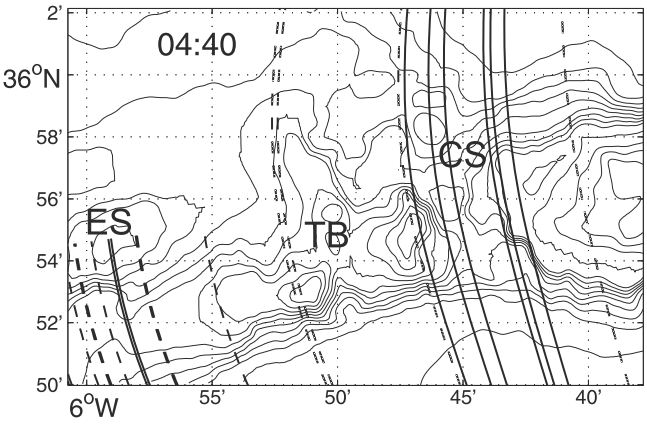

Figure 9. Sections of the strait where hydraulic transitions occur at t = 04:40 for the first (thick solid lines) and second baroclinic modes (thick dashed lines) according to three-layer hydraulic theory. Thin solid lines represent bottom depth contours (isobaths 50, 100, 150 m, etc.).

layer thickness and velocity [*Pratt*, 2008; *Sannino et al.*, 2009]

$$G_w^2 = \frac{u_1^2}{\frac{1}{w_I}\int_Y \frac{g'D_1}{u_1^2}} + \frac{u_2^2}{\frac{1}{w_I}\int_Y \frac{g'D_2}{u_2^2}}, \quad (3)$$

where w_I is the channel width at the interface depth, and $\int_Y$ denotes across-channel integral.

[27] The locations of sections of critical flow with respect to G_w^2 are indicated by solid lines in Figure 6f. They indicate subcritical flow $G_w^2 < 1$ to the east and west of the general area surrounding CS and including the upstream hydraulic jump. As one moves from west to east through this region, several transitions between subcritical and supercritical flow occur, possibly because of the irregular nature of the flow caused by numerous, short-wave disturbances generated by topography. The main conclusion that one should draw from this is that the exchange flow is hydraulically controlled, though it is difficult to interpret this in terms of classical hydraulic theory.

3.1.3. Baroclinic Wavefield Over TB and ES

[28] Although prominent surface signatures related to the baroclinic field are mainly found in the CS area (Figure 4), the internal dynamics are also remarkable in TB and ES. The weak surface trace left by internal hydraulic jumps in these areas is attributable to the great depth of the pycnocline (smaller current velocity associated to internal disturbances in the thick upper layer than in the bottom layer) downstream CS, especially over ES, as is shown below.

[29] Figure 8 shows isopycnals and velocity currents evolution along section S_1 (Figure 4). Even at slack tide two additional internal hydraulic jumps are apparent downstream CS (Figure 8a). The clearest hydraulic transition occurs over the ES crest, where isopycnals abruptly plunge over the western flank. The density field downstream the downslope flow shows a bulge of isopycnals, a clear signal of mixing taking place in the internal hydraulic jump formed at the lee side of the sill. The second hydraulic jump, less apparent, is formed in TB in the proximity of a secondary sill west of CS (SS; ~5°50′W).

[30] Increase of tidal forcing enhances velocity shear in TB and water mixing (Figures 8b and 8c). The flow at that time is potentially unstable as shown by the values of the Richardson number reaching $Ri < 1/4$ (shaded contours) throughout TB, suggesting the development of shear instabilities. Evidence of shear flow instabilities was reported by *Wesson and Gregg* [1994], who observed Kelvin-Helmholtz billows with 30–75 m horizontal scale. Such structures are too small to be resolved by the model, but additional unstable short waves develop and leave the irregular surface pattern immediately west of CS (Figure 4). These waves exist under strongly sheared flow, and vanish as soon as the tidal flow weakens. Along with these unstable waves, two disturbances with longer spatial scale and larger amplitudes appear in TB. They are characterized by a vertical structure with counterphase isopycnal displacements, thus classified as second-mode baroclinic modes. They are observed at a late stage of the flood cycle at the lee side of CS and the secondary sill (thick dashed lines in Figure 8) and propagate to the Mediterranean when tidal flow starts reversing.

[31] At first glance these structures may also be regarded as pools of mixed water advected by the background current. It is difficult to discern in practice whether these structures are waves or advected pools of mixed water, however, second-mode propagating LAIWs have been already observed in the strait [*Farmer and Armi*, 1988; *Armi and Farmer*, 1988]. *Vázquez et al.* [2006] also reported a multimodal structure of the internal wavefield with a simpler numerical model, thus supporting the idea that these moving structures are indeed internal waves. Further proof is provided by estimating the flow criticality by means of a three-layer approximation of the stratified flow, as done by *Sannino et al.* [2009], who considered an interfacial mixed layer. In the three-layer system two baroclinic modes are possible, and the criticality of the flow can be evaluated for both types of disturbances (see Appendix B). Figure 9 shows internal hydraulic transitions in the three-layer system at t = 04:40 h. Solid and dashed lines indicate transitions for the first and second internal modes, respectively. Hydraulic transitions for the first mode occur in CS and ES, whereas in TB hydraulic transitions are found for the second mode only. This is in line with the simulated character of the flow, and reinforces the idea that the structures found in TB are not advected pools of mixed water, but second-mode internal hydraulic jumps that propagate when the flow relaxes.

3.2. Strong Tidal Forcing: Spring Tides

[32] In this section we examine the baroclinic response during spring tides looking at a tidal cycle of $Tr_{\max}$ = 5.35 Sv (Figure 10). This is in the limit of maximum barotropic tidal flows occurring in the Strait of Gibraltar. It should be noted, however, that in practice, barotropic flows can be up to 1 Sv larger as a result of an additional net barotropic flow induced by meteorological forcing because of differences in atmospheric pressure over the Atlantic and the Mediterranean [*Candela et al.*, 1989].

[33] The surface pattern of velocity gradients shows a response of the baroclinic field during the early stage of the flood tide similar to the one previously described,

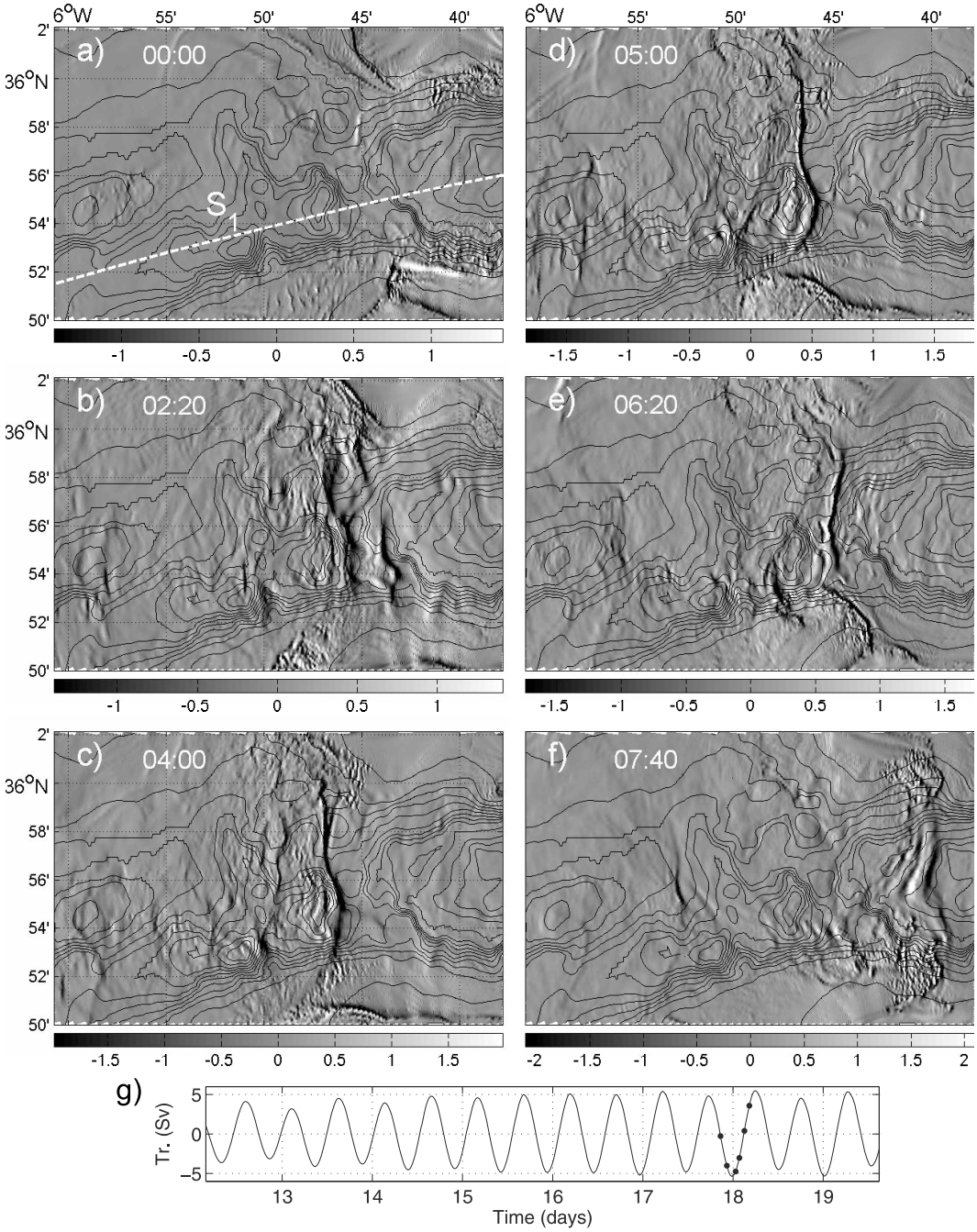

Figure 10. Same as Figure 4 for strong tidal forcing.

characterized by the formation of cross waves close to the lateral boundaries of the strait and two main wavefronts in the center of the channel. This configuration does not last to the ebb tide though, as further increase of tidal currents sweeps the two fronts to the lee side of CS to form a single internal hydraulic jump (Figure 10c). Moreover, an additional surface signature arises in TB over the secondary sill west of CS.

[34] Estimate of the flow criticality shows that the flow is locally supercritical from a few km east CS to its lee side (Figure 11), thus the crest-controlled state is lost in this case. Further downstream the flow is locally supercritical in many areas of TB, especially nearby the secondary sill (∼5°49′W, 36°54′W). The flow as a whole is, in fact, critical over that sill. This hydraulic configuration finds excellent correspondence with the wave behavior shown along section S_1 (Figure 12). The sequence shows how the upstream internal bore is swept to the lee side of the sill while another first-mode internal hydraulic jump appears at the lee side of the small obstacle. At that time three outstanding jumps are present: one at the lee side of CS, and the two associated to the secondary sill and ES. Note, however, that all major disturbances formed in TB vanish when tidal flow weakens, and the only jump that produces noticeable propagating waves is the one formed at the lee side of CS, which evolves into a series of internal solitary waves (Figure 13).

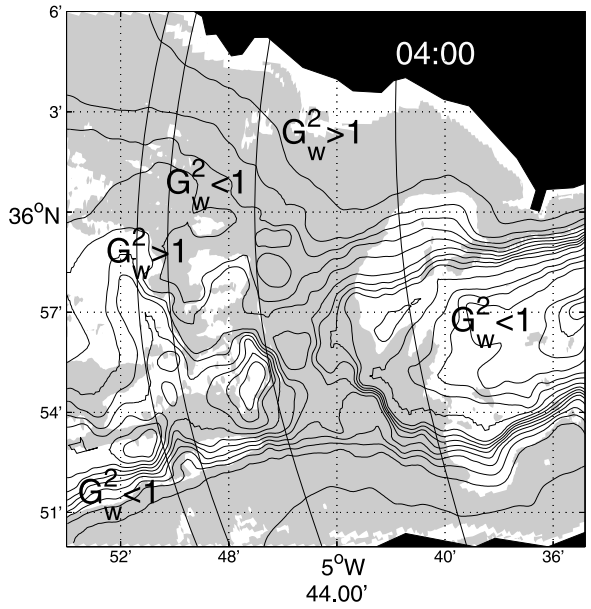

Figure 11. Same as Figure 6f for strong tidal forcing.

[35] The disappearance of the short waves associated to the hydraulic jump at the lee side of the secondary sill can be explained by the instability ($Ri < 1/4$) of the surrounding medium. Waves over that sill are unstable waves that only develop in the strongly sheared unstable flow. Their energy is either lost or transferred to mixing, as shown by the eroded stratification resulting in the area where they developed (compare Figures 12b and 12d). The above also applies to the short-scale unstable waves found in TB under moderate tidal forcing, and also to the short-scale disturbances observed at the lee side of ES in this case (see Figures 12c–12e). Stable waves are only possible when velocity shear relaxes as tidal flow start reversing. At that time a pair of second-mode internal waves are seen progressing to the Alboran Sea (see dashed lines in Figures 12d and 12e). The westernmost wave (located at $\theta \sim 5°53'$W) is also observed under moderate forcing and it was classified as a second-mode internal bore. The wave located farther upstream, suddenly appearing nearby CS when the first-mode hydraulic jump passes over the sill, has a different genesis. This second-mode wave is generated by wave-topography interaction. Such a process of energy cascade from first to higher-order baroclinic modes is well known and has been reported in several papers [see, e.g., *Vlasenko and Hutter*, 2001].

[36] Figure 13 shows the wave evolution during the ebb tide and reveals that a hydraulic jump is generated in CS in this stage of the tidal cycle. This jump, not apparent under moderate tidal forcing, is much weaker than the one formed with flood currents, and does not lead to westward propagating LAIWs. This asymmetry in the baroclinic response with the flood and ebb tides is observed in SAR images [*Jackson and Apel*, 2004].

[37] The last remark on Figure 13 concerns the eastward propagating wave packet generated during the flood tide. In the early stage of its evolution it consists of a rank-ordered group of internal solitary waves exceeding 100 m amplitude. The rank-ordered structure, with wave amplitudes decreasing from the front to the tail, is the expected configuration of a wave packet resulting from the nonlinear evolution of an internal bore [*Whitham*, 1974]. This configuration is caused by the nonlinear dispersion (waves of larger amplitudes propagate faster). However, in our case the regular structure of the wave packet breaks down as it enters Tarifa Narrows. *Vlasenko et al.* [2009] showed observational evidence of this evolution, and proved that the phenomena is driven by subsequent interactions of the LAIWs with the irregular bottom topography and lateral boundaries of the strait, which leads to a mechanism of energy-exchange between waves through energy radiation.

4. Discussions and Conclusions

[38] We present here a numerical experiment to examine the generation of nonlinear internal waves in the Strait of Gibraltar. The most important novelty introduced with respect to previous studies is the 3-D approach of the issue, an important characteristic in this place of the World Ocean where bottom topography is rather irregular, and both background stratification and barotropic tidal currents are quite spatially dependent. Available SAR images like the one shown in Figure 1 suggest the relevance of 3-D effects.

[39] The 1 month numerical experiment simulates the baroclinic response under the whole spectrum of possible tidal forcing in the area. Upon analyzing the bulk of numerical results we distinguish two types of tidal forcing with regards to the baroclinic response during the flood tide: the moderate tidal forcing, which approximately occurs in the range 3 Sv $< Tr_{max} <$ 4 Sv, and the strong tidal forcing taking place during spring tides when $Tr_{\max} >$ 4 Sv.

[40] Under moderate tidal forcing the baroclinic field over CS presents a fairly complex structure which includes oblique jumps and cross waves in shallow areas, two upstream internal hydraulic jumps, and a steep plunging pycnocline at the lee side of the sill. These structures may appear aligned together across the channel, thus apparently forming the same object when looking at the surface pattern captured by remote sensing images.

[41] Estimate of the flow criticality as a whole shows that a subcritical-to-supercritical hydraulic transition occurs east (upstream) of the sill, further west the flow turns to subcritical where two upstream hydraulic jumps develop, and recovers the definitive supercritical regime after passing through the sill crest again. A similar flow configuration but with a single upstream hydraulic jump was reported by *Cummins et al.* [2006] in the sill of Knigh Inlet (British Columbia, Canada), treated as a 2-D setting.

[42] The flow as a whole can be considered as a transition between the crest-controlled and the approach-controlled flow, two basic steady flow states reported by *Lawrence* [1993], who conducted a series of laboratory experiments of two-layer flows over an obstacle. The approach-controlled flow is characterized by a control section somewhere at the beginning (upstream) of the sill whose specific position depends on friction forces. Downstream the flow remains internally supercritical up to some point at the lee side of the sill, where it returns to a subcritical state through an internal hydraulic jump. The jump occurs immediately downstream of a steep plunge of the interface at the lee side of the obstacle, termed supercritical leap. Another distinctive

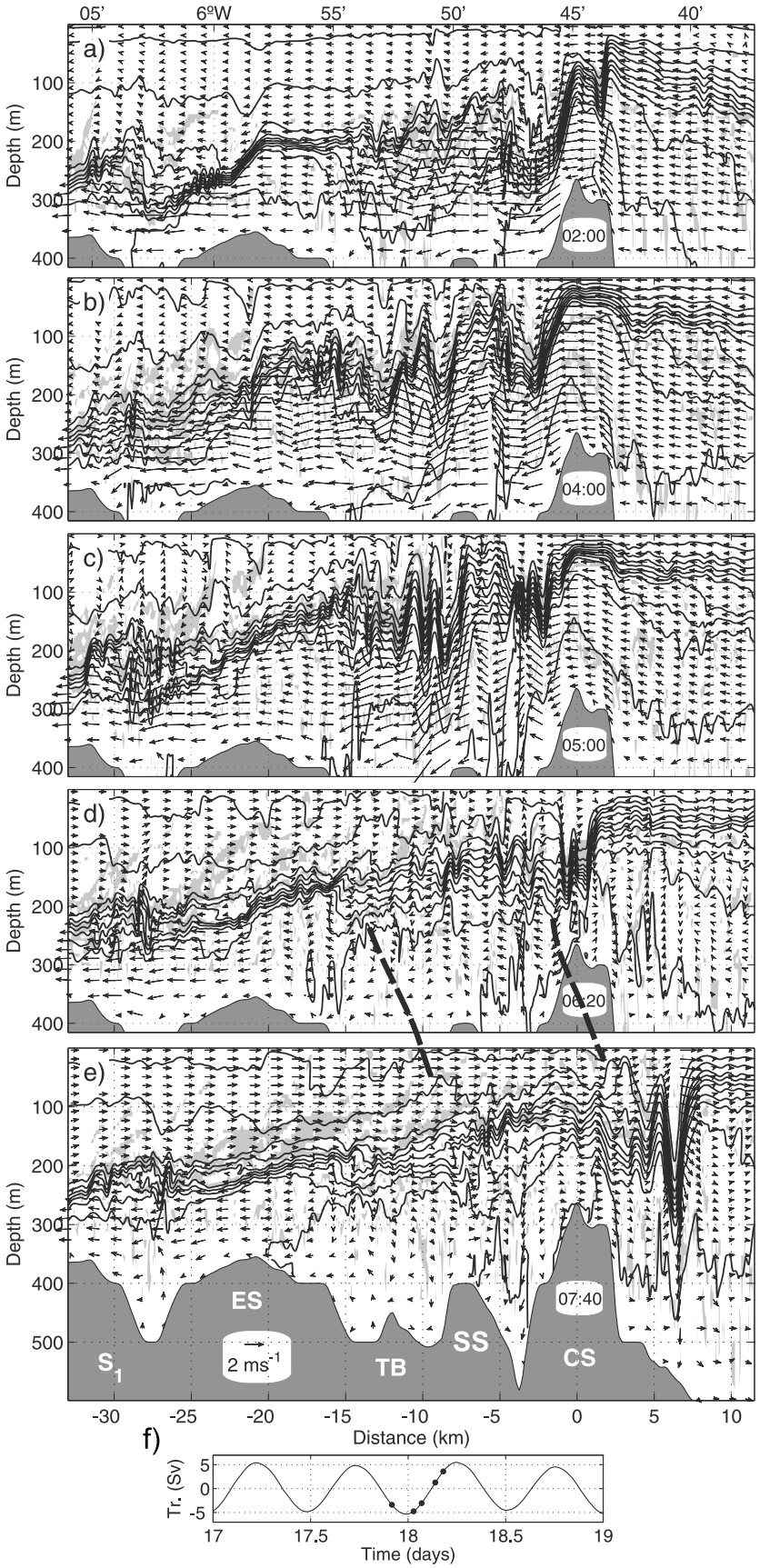

Figure 12. Same as Figure 8 for strong tidal forcing.

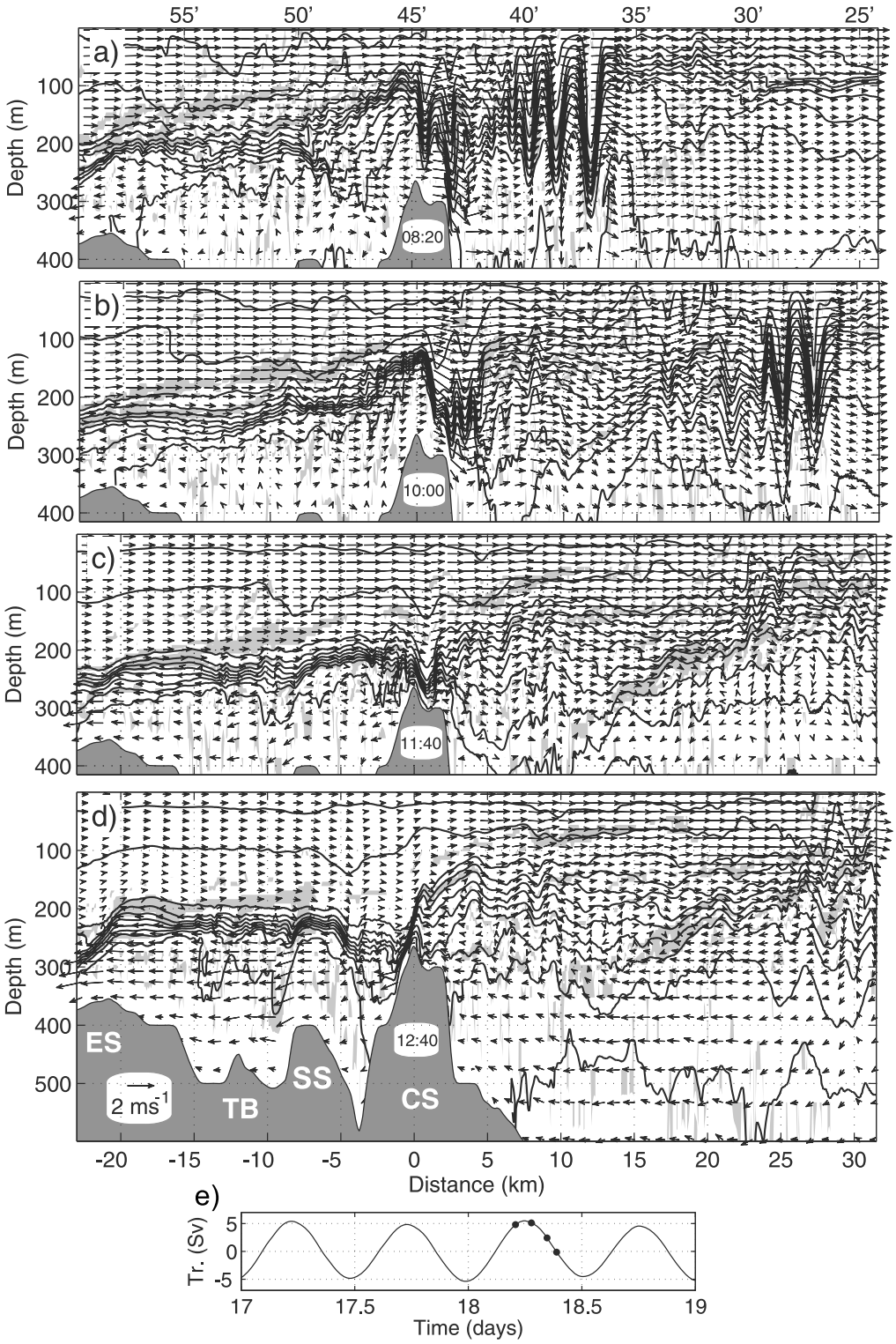

Figure 13. Extension of Figure 12 to the ebb tide.

feature of the approach-controlled flow is the rising slope of the pycnocline as it approaches the sill crest from the upstream side (from east to west in the present case). The flow under moderate forcing described here clearly shows this feature (Figures 5b, 8b, and 8c). However, some hydraulic transitions to subcritical state occur upstream of the sill and the flow nearby the sill crest remains critical. This last feature is distinctive of a crest-controlled flow. Therefore, the flow can be seen as a transient between these two steady states, characterized by the occurrence of the

upstream internal hydraulic jumps, eventually evolving into a series of propagating solitary waves.

[43] *Cummins et al.* [2006] discuss, in the case of Knight Inlet sill, whether the state with the upstream internal bore is a transient between two steady states or it is a steady state itself, a hybrid flow between the crest-controlled and the approach-controlled flow (obtained under stronger barotropic forcing). They found that for certain background stratification the upstream internal bore remained stationary under constant barotropic flow, thus suggesting the existence of a hybrid steady state. It is beyond the scope of this paper to discern whether the state with an upstream internal bore in Gibraltar is a transient between two steady flows, or rather a steady state itself. However, it is worth noting that the quasi-steady approximation of the flow over CS is very questionable, thus it is unlikely that the flow state characterized by the upstream internal bore constitutes indeed a steady state configuration. The quasi-steady approximation requires a time scale for the tidal forcing much smaller than the time scale required for the flow to adjust to the obstacle. As long as the flow adjustment is carried out via internal waves, the quasi-steady approximation is valid whenever $cT/L \ll 1$, where c is the propagation velocity of an internal wave, T the time scale of the barotropic forcing variability, and L the length scale of the obstacle. For the flow over CS; $c \sim 1$ ms^{-1}, $T \sim 10^4$ s, and $L \sim 10^4$ m; thus $cT/L \sim 1$ and the quasi-steady approximation breaks down.

[44] Under strong tidal forcing (spring tides) the upstream internal bores are swept down to the lee side of the sill, and the flow acquires the hydraulic configuration of a pure approach-controlled state, now with the supercritical region extending from the upstream control section to a few hundred meters downstream CS crest. Toward the end of flood tide the internal hydraulic jump formed at the lee side of the sill, matching supercritical and subcritical condition in TB, evolves into a series of LAIWs exceeding 100 m amplitude. This time-dependent response to strong tidal forcing has been also observed in Knight Inlet [*Stashchuk and Vlasenko*, 2007; *Cummins and Armi*, 2010]. However, differently to Gibraltar, these field observations and numerical studies in the sill area of Knight Inlet indicate that the approach-controlled flow scenario does not occur with fortnightly periodicity, but it is rather a seasonal phenomena typical of winter time, when the intensity of tidal forcing increases as the background stratification weakens (larger values of the composite Froude number due to smaller reduced gravity).

[45] It is important to remark that the hydraulic control found under moderate and strong tidal forcing east of the CS is distinct from the exit control occurring during some stages of the ebb tide [*Sannino et al.*, 2009]. The exit control occurs further east close to the narrowest section of the strait, and isolates the exchange flow from internal perturbations coming from the Mediterranean.

[46] Further examination of model results reveal that additional internal hydraulic jumps occur in ES and nearby smaller obstacles in TB. These regions are very prompt to the development of shear instabilities in most parts of the tidal cycle, as suggested by the low value of the Richardson number [see also *Wesson and Gregg*, 1994]. This seems to be the reason why major stable propagating waves are not found in the area, and only a system of second-mode internal waves is observed when the tidal flow and velocity shear slacken.

Appendix A: The Significance of the Local Value of G^2

[47] Consider a two-layer flow with upper and lower layer velocities (U_1, V_1) and (U_2, V_2), and layer thicknesses H_1 and H_2. We consider the possibility that a small-amplitude, stationary disturbance with velocity, interface height and rigid-lid pressure perturbations (u_1, v_1), (u_2, v_2), η, and p exist. The disturbance is assumed to vary on a small scale compared to the scale of variations of the background flow, and the latter may thus be approximated as uniform on the scale of the perturbation. The governing linearized equations are then

$$\begin{aligned} U_1 u_{1x} + V_1 u_{1y} &= -p_x/\rho \\ U_1 v_{1x} + V_1 v_{1y} &= -p_y/\rho \\ U_2 u_{2x} + V_2 u_{2y} &= -p_x/\rho - g'\eta_x \\ U_2 v_{2x} + V_2 v_{2y} &= -p_y/\rho - g'\eta_y \\ H_1 u_{1x} + H_1 v_{1y} - U_1\eta_x - V_1\eta_y &= 0 \\ H_2 u_{2x} + H_2 v_{2y} + U_2\eta_x + V_2\eta_y &= 0 \end{aligned}$$

If we now look for a disturbance in which each perturbation variable is proportional to $\sin(kx - ly)$, then the subsequent problem can be written in the matrix form $Mb = 0$, where

$$b = \Big(u_1/(g'H_1)^{1/2}, v_1/(g'H_1)^{1/2}, u_2/(g'H_1)^{1/2}, v_2/(g'H_1)^{1/2}, \cdot\, \eta/H_1, p/g'\rho H_1\Big)^T$$

and

$$M = \begin{pmatrix} \alpha\tilde{U}_1 + \tilde{V}_1 & 0 & 0 & 0 & 0 & \alpha \\ 0 & \alpha\tilde{U}_1 + \tilde{V}_1 & 0 & 0 & 0 & 1 \\ 0 & 0 & \gamma^{1/2}\big(\alpha\tilde{U}_2 + \tilde{V}_2\big) & 0 & \alpha & \alpha \\ 0 & 0 & 0 & \gamma^{1/2}\big(\alpha\tilde{U}_2 + \tilde{V}_2\big) & 1 & 1 \\ \alpha & 1 & 0 & 0 & -\big(\alpha\tilde{U}_2 + \tilde{V}_2\big) & 0 \\ 0 & 0 & \alpha\gamma & \gamma & \gamma^{1/2}\big(\alpha\tilde{U}_2 + \tilde{V}_2\big) & 0 \end{pmatrix},$$

where $\big(\tilde{U}_1, \tilde{V}_1\big) = (U_1,V_1)/(g'H_1)^{1/2}$, $\big(\tilde{U}_2, \tilde{V}_2\big) = (U_2,V_2)/(g'H_2)^{1/2}$, $\alpha = k/l$ and $\gamma = H_2/H_1$.

[48] Nontrivial solutions require $\det(M) = 0$ and this gives a condition between the background flow and the slope α of the lines of constant phase of the disturbance. We now simplify the analysis to a background flow in which the upper and lower layer velocity vectors point in the same direction, or in opposite directions. With no loss of generality we

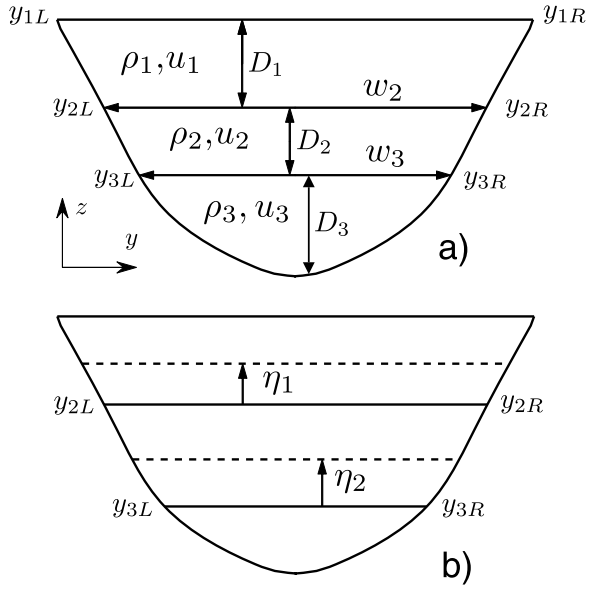

Figure B1. Definition sketch of a three-layer flow. (a) Unperturbed state and (b) perturbed interfaces elevation.

choose alignment along the x axis, and thus, $V_1 = V_2 = 0$. Taking $\det(M) = 0$ then leads, after a little algebra, to

$$\tilde{U}_1^2 + \tilde{U}_2^2 = \frac{1+\alpha^2}{\alpha} = \frac{U_1^2}{g'H_1} + \frac{U_2^2}{g'H_2}.$$

[49] The term on the right-hand side is the composite Froude number G^2 for 2D flow. It is clear that $G^2 \geq 1$ in order for stationary disturbances to exist, and also that a stationary disturbance corresponding to a unique value of α^2 is possible for any $G^2 \geq 1$. The disturbance consists of two cross waves with slope $\pm\alpha$.

[50] For the case in which the upper and lower layer velocities are not aligned, a similar calculation leads to the condition

$$\left(\alpha\tilde{U}_1 + \tilde{V}_1\right)^2 + \left(\alpha\tilde{U}_2 + \tilde{V}_2\right)^2 = 1 + \alpha^2,$$

which with $\alpha = k/l$ can be written as

$$\left(\frac{(U_1, V_1)}{g'H_1} \cdot \frac{\vec{k}}{\left|\vec{k}\right|}\right)^2 + \left(\frac{(U_2, V_2)}{g'H_2} \cdot \frac{\vec{k}}{\left|\vec{k}\right|}\right)^2 = 1.$$

[51] In other words, the composite Froude number based on the components of the upper and lower layer velocities in the direction of the wave number vector $\vec{k} = (k, l)$, i.e., perpendicular to the wave crests, must be unity for a stationary disturbance to exist.

Appendix B: Three-Layer Critical Flow: Mode Relations

[52] The three-layer system consists of the Atlantic upper layer, the Mediterranean bottom layer, and an interfacial mixed layer (see details of the three-layer definition and separation given by *Sannino et al.* [2009]). The criticality of the flow is evaluated following *Pratt* [2008], who derived a general condition for the criticality of a layered flow when layers thickness and velocities vary across the channel. Consider the three-layer flow sketched in Figure B1, the critical condition is

$$\tilde{F}_1^2 + \left(\frac{1-r}{r} + \frac{w_3}{w_2}\right)\tilde{F}_2^2 + \tilde{F}_3^2 - \frac{w_3}{w_2}\tilde{F}_1^2\tilde{F}_2^2 - \tilde{F}_1^2\tilde{F}_3^2 - \frac{1-r}{r}\tilde{F}_2^2\tilde{F}_3^2 = 1, \quad \text{(B1)}$$

where

$$\tilde{F}_1^2 = \left(\frac{1}{w_2}\int_{y_1L}^{y_1R} \frac{g'_{21}D_1}{u_1^2}dy_1\right)^{-1},$$
$$\tilde{F}_2^2 = \left(\frac{1}{w_2}\int_{y_2L}^{y_2R} \frac{g'_{32}D_2}{u_2^2}dy_2\right)^{-1},$$
$$\tilde{F}_3^2 = \left(\frac{1}{w_3}\int_{y_3L}^{y_3R} \frac{g'_{32}D_3}{u_3^2}dy_3\right)^{-1},$$

$g'_{21} = g(\rho_2 - \rho_1)/\bar{\rho}$, $g'_{32} = g(\rho_3 - \rho_2)/\bar{\rho}$, and $r = (\rho_2 - \rho_1)/(\rho_3 - \rho_1)$. When the critical condition (B1) is fulfilled, one of the four velocities of the two possible long-wave baroclinic modes (a pair velocity values for each mode), satisfying appropriate bottom and sidewall boundary conditions, becomes null. It is not possible to discern the vertical structure of the internal mode that makes the flow critical, that is, whether if the associated interface oscillations are in phase or counterphase.

[53] To elucidate this issue, consider $\tilde{d}_1$ and $\tilde{d}_2$ layer thickness perturbations of the background state. In terms of perturbations of interface elevation η_1 and η_2, thickness perturbations are given by

$$\tilde{d}_1 = -\eta_1,$$
$$\tilde{d}_2 = \eta_1 - \eta_2.$$

Following *Pratt* [2008], the condition of flow criticality is equivalent to the existence of nontrivial solutions of the following system of linear equations:

$$\begin{pmatrix} -w_2 & 0 & f_1 \\ w_2 - w_3 - g'_{2,1}f_2 & -w_3 & f_2 \\ w_3 - g'_{3,1}f_3 & w_3 - g'_{3,2}f_3 & f_3 \end{pmatrix} \begin{pmatrix} \tilde{d}_1 \\ \tilde{d}_2 \\ \tilde{p}_T \end{pmatrix} = 0, \quad \text{(B2)}$$

where

$$f_n = \int_{y_{nL}}^{y_{nR}} \left(\frac{D_n}{u_n^2}\right)dy,$$
$$g'_{n,i} = [(\rho_n - \rho_i)/\bar{\rho}]g,$$

and $\tilde{p}_T$ is the rigid-lid pressure perturbation divided by the mean density $\bar{\rho}$. Since solutions exist, we can use the first two equations of (B2) to obtain a relationship between $\tilde{d}_1$ and $\tilde{d}_2$. Elimination of $\tilde{p}_T$ gives

$$\left[\frac{w_2}{f_1} + \frac{w_2 - w_3 - g'_{2,1}f_2}{f_2}\right]\tilde{d}_1 = \frac{w_3}{f_2}\tilde{d}_2.$$

After expressing $\tilde{d}_1$, $\tilde{d}_2$ in terms of η_1, η_2 and some algebra, the following relation between the perturbations of interface elevation is found:

$$\eta_2 = \alpha \cdot \eta_1, \tag{B3}$$

where

$$\alpha = \frac{w_2}{w_3 \tilde{F}_2^2}\left[\frac{r}{1-r}\left(\tilde{F}_1^2 - 1\right) + \tilde{F}_2^2\right],$$

$$\tilde{F}_1^2 = \frac{1}{\frac{g'_{2,1}}{w_2} f_1}, \quad \tilde{F}_2^2 = \frac{1}{\frac{g'_{3,2}}{w_2} f_2},$$

and $r = (\rho_2 - \rho_1)/(\rho_3 - \rho_1)$.

[54] Now it is straightforward to distinguish which of the two internal modes makes the flow critical. Following equation (B3), if $\alpha > 0$ the two interface perturbations are in phase, and we say that the first baroclinic mode makes the flow critical. In opposite case, if $\alpha < 0$, the two interface perturbations are in counterphase, and it is the second baroclinic mode that makes the flow critical. It is important to remark that the classification of the first and second baroclinic modes is strictly made in terms of the wave vertical structure and is not based on their propagation velocity. In absence of velocity shear the first mode (in-phase vertical isopycnal displacements) propagates faster than the second baroclinic mode (counterphase vertical isopycnal displacements), but this is not necessarily true when shear is present.

[55] **Acknowledgments.** This work is a contribution to the Spanish-funded National Project INGRES-2 (CTM2006-02326). Partial financial support from Acción Complementaria CTM2009-05810/E (Spanish Ministry of Science and Innovation) and project P08-RNM-3738 from Plan Andaluz de Investigación (Andalucia regional government) is acknowledged. We are grateful to the CRESCO supercomputing facilities located at ENEA (http://www.cresco.enea.it). The SAR image shown in Figure 1 was kindly provided by the European Space Agency (Envisat ASAR Data, project AO.SMOS4657: Key Mediterranean Sea Oceanographic Processes Estimated Through Remote-Sensed Data). The authors are also thankful to two anonymous referees for helpful comments and suggestions.

References

Alpers, W. (1985), Theory of radar imaging of internal waves, *Nature*, *314*, 245–247.

Armi, L. (1986), The hydraulics of two flowing layers with different densities, *J. Fluid Mech.*, *163*, 27–58.

Armi, L., and D. M. Farmer (1988), The flow of Atlantic Water through the Strait of Gibraltar, *Prog. Oceanogr.*, *21*(1), 1–105.

Armi, L., and D. Farmer (2002), Stratified flow over topography: Bifurcation fronts and transition to the uncontrolled state, *Proc. R. Soc. London, Ser. A*, *458*, 513–538.

Brandt, P., W. Alpers, and J. Backhaus (1996), Study of the generation and propagation of internal waves in the strait of Gibraltar using a numerical model and synthetic aperture radar images of the European ERS1 satellite, *J. Geophys. Res.*, *101*, 14,237–14,252.

Brandt, P., A. Rubino, W. Alpers, and J. O. Backhaus (1997), Internal waves in the Strait of Messina studied by a numerical model and synthetic aperture radar images from the ERS 1/2 satellites, *J. Phys. Oceanogr.*, *27*, 648–663.

Bryden, H. L., and T. H. Kinder (1991), Steady two-layer exchange through the Strait of Gibraltar, *Deep Sea Res. Part I*, *38*, S445–S463.

Candela, J., C. Winant, and H. L. Bryden (1989), Meteorologically forced subinertial flows through the strait of Gibraltar, *J. Geophys. Res.*, *94*, 12,667–12,674.

Candela, J., C. Winant, and A. Ruiz (1990), Tides in the Strait of Gibraltar, *J. Geophys. Res.*, *95*, 7313–7335.

Carter, G. S., and M. A. Merrifield (2007), Open boundary conditions for regional tidal simulations, *Ocean Modell.*, *18*, 194–209.

Chow, V. T. (1959), *Open-Channel Hydraulics*, McGraw-Hill, New York.

Cummins, P., and L. Armi (2010), Upstream internal jumps in stratified sill flow: Observations of formation, evolution, and release, *J. Phys Oceanogr.*, *40*, 1419–1426.

Cummins, P. F., L. Armi, and S. Vagle (2006), Upstream internal hydraulic jumps, *J. Phys. Oceanogr.*, *36*, 753–769.

Farmer, D. M., and L. Armi (1988), The flow of Mediterranean Water through the Strait of Gibraltar, *Prog. Oceanogr.*, *21*(1), 1–105.

García Lafuente, J., J. L. Almazán, F. Fernández, A. Khribeche, and A. Hakimi (1990), Sea level in the Strait of Gibraltar: Tides, *Int. Hydrogr. Rev.*, *67*(1), 111–130.

García Lafuente, J., J. M. Vargas, F. Plaza, T. Sarhan, J. Candela, and B. Bascheck (2000), Tide at the eastern section of the Strait of Gibraltar, *J. Geophys. Res.*, *105*, 14,197–14,213.

García Lafuente, J., A. Sánchez Román, G. Díaz del Río, G. Sannino, and J. C. Sánchez Garrido (2007), Recent observations of seasonal variability of the Mediterranean outflow in the Strait of Gibraltar, *J. Geophys. Res.*, *112*, C10005, doi:10.1029/2006JC003992.

Hundsdorfer, W., B. Koren, M. van Loon, and J. G. Verwer (1995), A positive finite-difference advection scheme, *J. Comput. Phys.*, *117*, 35–46.

Jackson, C. R., and J. Apel (2004), An atlas of internal solitary-like waves and their properties, 2nd ed., report, Global Ocean Assoc., Alexandria, Va. [Available at http://www.internalwaveatlas.com/.]

Lawrence, G. A. (1993), The hydraulics of steady two-layer flow over a fixed obstacle, *J. Fluid Mech.*, *254*, 605–633.

Leith, C. E. (1968), Diffusion approximation for two-dimensional turbulence, *Phys. Fluids*, *10*, 1409–1416.

Marshall, J., C. Hill, L. Perelman, and A. Adcroft (1997a), Hydrostatic, quasi-hydrostatic, and nonhydrostatic ocean modeling, *J. Geophys. Res.*, *102*, 5733–5752.

Marshall, J., A. Adcroft, C. Hill, L. Perelman, and C. Heisey (1997b), A finite-volume, incompressible Navier Stokes model for studies of the ocean on parallel computers, *J. Geophys. Res.*, *102*, 5753–5766.

MEDAR Group (2002), *Medatlas 2002: Mediterranean and Black Sea Database of Temperature, Salinity and Bio-Chemical Parameters Climatological Atlas*, Eur. Comm. Mar. Sci. and Technol. Programme, Paris.

NOAA (2006), ETOPO2v2 Global Gridded 2-Minute Database, http://www.ngdc.noaa.gov/mgg/global/etopo2.html, Natl. Geophys. Data Cent., Boulder, Colo.

Pacanowski, R. C., and S. G. H. Philander (1981), Parameterisation of vertical mixing in numerical models of tropical oceans, *J. Phys. Oceanogr.*, *11*, 1443–1451.

Pratt, L. (2008), Critical conditions and composite Froude numbers for layered flow with transverse variations in velocity, *J. Fluid Mech.*, *602*, 241–266.

Richez, C. (1994), Airborne synthetic aperture radar tracking of internal waves in the Strait of Gibraltar, *Prog. Oceanogr.*, *33*, 93–159.

Sánchez-Garrido, J. C., J. García Lafuente, F. Criado Aldeanueva, A. Baquerizo, and G. Sannino (2008), Time-spatial variability observed in velocity of propagation of the internal bore in the Strait of Gibraltar, *J. Geophys. Res.*, *113*, C07034, doi:10.1029/2007JC004624.

Sánchez-Román, A., G. Sannino, J. García Lafuente, A. Carillo, and F. Criado-Aldeanueva (2009), Transport estimates at the western section of the Strait of Gibraltar: A combined experimental and numerical modeling study, *J. Geophys. Res.*, *114*, C06002, doi:10.1029/2008JC005023.

Sannino, G., L. Pratt, and A. Carillo (2009), Hydraulic criticality of the exchange flow through the Strait of Gibraltar, *J. Phys. Oceanogr.*, *39*, 2779–2799, doi:10.1175/2009JPO4075.1.

Sanz, J. L., J. Acosta, M. Esteras, P. Herranz, C. Palomo, and N. Sandoval (1991), Prospección geofísica del Estrecho de Gibraltar (resultados del programa Hércules 1980–1983), *Publ. Espec. Inst. Esp. Oceanogr.*, *7*, 48 pp., Span. Inst. of Oceanogr., Madrid.

Stashchuk, N., and V. Vlasenko (2007), Numerical modelling of stratified tidal flow over a Fjord Sill, *Ocean Dyn.*, *57*, 325–338, doi:10.1007/s10236-007-0112-7.

Vázquez, A., N. Stashchuk, V. Vlasenko, M. Bruno, A. Izquierdo, and P. C. Gallacher (2006), Evidence of multimodal structure of the baroclinic tide in the Strait of Gibraltar, *Geophys. Res. Lett.*, *33*, L17605, doi:10.1029/2006GL026806.

Vlasenko, V. I., and K. Hutter (2001), Generation of second mode solitary waves by the interaction of a first mode soliton with a sill, *Nonlinear Processes Geophys.*, *8*, 223–239.

Vlasenko, V., J. C. Sánchez Garrido, N. Stashchuk, J. García Lafuente, and M. Losada (2009), Three-dimensional evolution of large-amplitude internal waves in the Strait of Gibraltar, *J. Phys. Oceanogr.*, *39*, 2230–2246.

Wesson, J. C., and M. C. Gregg (1994), Mixing at Camarinal Sill in the Strait of Gibraltar, *J. Geophys. Res.*, *99*, 9847–9878, doi:10.1029/94JC00256.

Whitham, G. B. (1974), *Linear and Nonlinear Waves*, John Wiley, New York.

Ziegenbein, J. (1969), Short internal waves in the Strait of Gibraltar, *Deep Sea Res.*, *16*, 479–487.

J. García Lafuente and J. C. Sánchez-Garrido, Grupo de Oceanografía Física, Departamento Física Aplicada II, University of Malaga, Campus de Teatinos s/n, E-29071 Malaga, Spain. (jcsanchez@ctima.uma.es)

L. Liberti, Istituto Superiore per la Protezione e la Ricerca Ambientale, via Curtatone 3, I-00185 Rome, Italy.

L. Pratt, Woods Hole Oceanographic Institution, Mail Stop 21, 360 Woods Hole Rd., Woods Hole, MA 02543, USA.

G. Sannino, Ocean Modeling Unit, Ente per le Nuove Tecnologie, l'Energia e l'Ambiente, via Anguillarese 301, I-00123 Rome, Italy.